3D Quantification Of Microstructural Properties Of Lini0.5Mn0.3Co0.2O2 High-Energy Density Electrodes By X-Ray Holographic Nano-Tomography

Tuan-Tu Nguyen, Julie Villanova, Zeliang Su, Rémi Tucoulou, Benoît Fleutot, Bruno Delobel, Charles Delacourt, Arnaud Demortière

3D Quantification Of Microstructural Properties Of $Lini_{0.5}Mn_{0.3}Co_{0.2}O_2$ High-Energy Density Electrodes By X-Ray Holographic Nano-Tomography

Tuan-Tu Nguyen[1,2], Julie Villanova[5], Zeliang Su[1], Rémi Tucoulou[5], Benoît Fleutot[1,3], Bruno Delobel[2], Charles Delacourt[1,3*], Arnaud Demortière[1,3,4*]

[1]Laboratoire de Réactivité et Chimie des Solides (LRCS), CNRS UMR 7314, Université de Picardie Jules Verne, Hub de l'Energie, Rue Baudelocque, 80039 Amiens Cedex, France.

[2]Renault Technocentre, 78084 Guyancourt, France

[3]Réseau sur le Stockage Electrochimique de l'Energie (RS2E), CNRS FR 3459, Hub de l'Energie, Rue Baudelocque, 80039 Amiens Cedex, France.

[4]ALISTORE-European Research Institute, CNRS FR 3104, Hub de l'Energie, Rue Baudelocque, 80039 Amiens Cedex, France.

[5]ESRF - The European Synchrotron, CS 40220, 38043, Grenoble Cedex 9, France

Corresponding Author:

Arnaud Demortière ✉: arnaud.demortiere@u-picardie.fr

Charles Delacourt ✉: charles.delacourt@u-picardie.fr

ABSTRACT:

Despite a significant progress in the field of tomography, capture the carbon binder domain morphology presented in the Li-ion electrode remains challenging, due to its low attenuation coefficient. In this work, quantitative phase contrast X-ray nano-holotomography is used as a straightforward approach that provides a large reconstructed volume, where the carbon binder domain can be resolved along with the active materials and the pore space. As a result, a complete quantitative analysis of the microstructures of three $LiNi_{0.5}Mn_{0.3}Co_{0.2}O_2$ high energy density electrodes, including the characterization of each phase separately along with the statistical quantification of their inter-connectivity at particle scale, is performed. The microstructural heterogeneities are

quantified and comparison between different electrodes is done. The results from this work suggest the negative impacts of the carbon binder domain excess to the electrode performance at high C-rates. Those results are true in the case of high energy density electrodes, and are due to the reduction of the electrochemical active surface area. This sheds light to the optimization of the electrode design to improve the power rate of high energy density electrodes.

KEYWORDS: lithium ion battery, electrode microstructure, X-ray holotomography, nanoCT, microstructure analysis.

Introduction

Over the last decades, with the increase of the energy demand along with the shift towards greener energy solutions, lithium-ion batteries have gained attraction for energy storage applications.[1]–[4] A lithium-ion battery is an electrochemical device that provides energy via electrochemical reactions that occur within the two porous electrodes: the anode and the cathode. Porous structures are widely used for making electrodes since they can massively increase the specific interfacial area between phases, which increases the accessible capacity of the active materials at high C-rates. However, the trade-off is the complexity of the electrode microstructure, as it adopts a hierarchical architecture.[5] Commonly, the electrode microstructure is a mixture of different phases: active materials (AM), additives such as mixture of conductive carbon (*e.g.,* C65) and binder (*e.g.,* PVdF), and pores, which are eventually filled with an electrolyte. This microstructure has been reported to play a crucial role in the performance of lithium-ion battery electrodes, as it affects the effective electronic/ionic transport properties through the morphology of the conducting matrix;[6]–[11] the electrochemical kinetics via the interfacial area between phases;[12][13] as well as the mechanical properties.[14] Hence, it is of particular importance to understand the interplay between the complex microstructure of a porous electrode and its electrochemical performance. In light of this, over the last years, tomography techniques have been significantly developed as a powerful tool to investigate the microstructure of the electrodes.[12][15]–[19] These techniques provide interesting quantitative and/or qualitative metrics that shed light on the effects of the microstructure on the final performance.[12][20]–[22] In particular, they allow for a spatial analysis of the distribution of the different phases within the electrode, which is not accessible from regular electrochemical measurements. Non-uniform distribution phases leading to microstructural heterogeneities, have been demonstrated to induce a non-uniform electrochemical behavior, which can deteriorate the final performance, and cause macroscopic failures.[14][23]–[27]

Focused ion beam scanning electron microscopy (FIB/SEM),[28]–[30] and transmission X-ray computed tomography (TXM CT) including µCT and nanoCT[18][27][31]–[35] are the most commonly used 3D techniques to study microstructure of batteries. The FIB/SEM

technique usually offers a higher spatial resolution (*ca.* 10 nm pixel size) compared to TXM CT, but only a small volume (*ca.* 10x10x10 μm^3) can be acquired under reasonable time and labor. Because the sample is sequentially milled while imaging, the technique is inherently destructive, preventing all subsequent studies of the microstructure if needed. In contrast, TXM CT offers a multiscale (from µ to nano) and nondestructive approach.[36] While TXM µCT offers a capability of analyzing large volumes such as the visualization of an entire device,[35] TXM nanoCT provides a spatial resolution below 100 nm allowing to access properties at micro-scale with a high reliability.[27] Depending on the materials, the trade-off between an appropriate resolution and a large volume (*i.e.* the representativeness) needs to be considered to obtain reliable results. Most of TXM CT experiments rely on the attenuation contrast, which increases with the density of the materials or the atomic number of the elements. Thus, low-*Z* materials such as the mixture of carbon conductive and binder, so-called the carbon binder domain in the porous electrode (CBD), have low attenuation. Then, the contrast of the CBD compared to pores in final images is weak. As a consequence, image analysis, especially the segmentation step, is challenging and in a majority of studies, CBD and pores cannot be resolved. Few studies based on TXM nanoCT have attempted to capture the three phases separately: AM, CBD, and pores. The common approach is to add a synthetic structure of CBD[29][37] to the AM framework obtained from the tomographic data. Although this approach offers the ability of adjustment of the CBD morphology,[38]–[40] the results stay somehow “fictive”. A more realistic approach is from Daemi *et al.,*[19] in which they combined the information from the FIB/SEM analysis of a stand-alone CBD electrode (*i.e.* prepared with no NMC particles). The use of a stand-alone CBD electrode was also used by Lu *et al.*[41] to capture features of the CBD using a novel TXM nanoCT dual-scan superimposition technique. The validity of the stand-alone CBD electrode might be questioned since the behavior of the CBD slurry during the manufacturing process might not be the same as when considering the presence of AM in the slurry. Recently, Müller *et al.*[42] proposed the multimodal approach combining TXM nanoCT data with data obtained using ptychographic X-ray CT. Impressively, this approach enables CBD to be clearly visualized, as the ptychographic technique offers higher spatial resolution (40 nm) along with a pixel size of 20 nm. However, combining different imaging techniques requires

significant effort for the sample preparation step, the imaging process and the post-processing data. As an innovative solution, Morelly *et al.*[43] proposed to replace the conventional carbon black by carbon-coated iron nanoparticles as contrast-enhancing particles, which allows resolving the CBD from the remaining. However, this approach cannot be applied for a wide range of industry-graded electrodes, as it still requires a supplementary step for making electrodes with specific additives.

Besides the attenuation contrast information, TXM CT also probes the phase contrast information, which relates to the refraction of the incident beam. Since the refraction index of a material can be thousand times greater than its absorption factor, phase contrast between weakly attenuating materials is enhanced. Taiwo *et al.* used the phase-contrast tomography to capture the microstructure of weakly-absorbant materials such as graphite, and obtained improved results compared to absorption-based images.[44] Su *et al.* used the Zernike phase contrast to capture the morphology of the Li_2O_2 in a Li-air electrode.[34] Moreover, the workflow is quite similar to the absorption-based technique, which enables a straightforward approach to obtain the 3D microstructure data.

In this study, the hard X-ray nano-holotomography technique illustrated in Figure 1a and available at the ID16B beamline of the ESRF is used[32][33] to extract microstructural properties of three different $LiNi_{0.5}Mn_{0.3}Co_{0.2}O_2$ (NMC) porous electrodes. This phase contrast technique allows the reconstruction of large 3D volumes (for those, the size can be up to 100x100x100 μm^3, see Figure 1b, c), while keeping a small pixel size (50 nm) for an adequate high spatial resolution and intensity contrast to distinguish the three domains: AM, CBD and pores. It is worth noting that the resolution of the holotomography technique might not be enough to capture the nano-porosity that can exist in the CBD clusters and that can only be captured by FIB/SEM technique (Figure S1). Given that this porosity can reach up to 47% within the CBD,[29] it can contribute significantly to electrochemical performance, as discussed by Trembacki *et al*.[40] and Ferraro *et al.*[45] using synthetic CBD morphology. Nevertheless, the holotomography technique still provides a persistent and high-throughput workflow to capture other microstructural details. Furthermore, the volumes examined with holotomography are relatively large, in

respect to the most prominent component within the electrodes, *i.e.* NMC particles (D_{50} = 4.6 µm). The representativeness can therefore be validated.

The discrimination of the morphology of the different phases within the electrode using a machine-learning segmentation method (Figure 1d, e) allows for a complete image-based analysis in order to investigate the effects of the microstructure on the electrode electrochemical performance. A statistical approach is frequently employed to determine microstructure inhomogeneities. It can be done by studying variations of different sub-volumes at different locations. In this study, beside the global analysis of the control volume, a statistical analysis at the particle scale (Figure 1f) including more than 500 individual NMC particles for each sample is proposed instead. It has been chosen because certain metrics are more relevant at particle scale, since they are related to the kinetics of the electrochemical reaction, which occurs at the interface between the AM particles and the electrolyte. This approach provides statistically-significant results that offer an insight into the distribution of the microstructural properties at particle scale. Finally, a scenario to comprehend the impact of the microstructure on the electrochemical performance (via discharge rate-capability measurements) of the three electrodes is proposed.

Results & Discussion

The results presented here after are based on a careful image processing of the 3D volumes obtained by X-ray nano-holotomography. All the steps of the image processing and data analysis are detailed in the 'Methods' section of this paper. It is worth noting: (i) that the representativeness of the control volumes used for the data analysis has been validated (Figure S3), (ii) that a machine learning algorithm (Random Forest via Trainable Weka plugin in ImageJ) has been used for the segmentation and (iii) that a global analysis of the control volume along with a statistical quantification of the inter-connectivity between phases at the particle scale are performed for the complete characterization of the microstructures.

Active material phase

As illustrated in Figure 1b-d, the NMC particles of the AM phase can be well-identified based on either the grey level (brightest region) or their morphology (*e.g.* “spherical”-type secondary particles). The volume fraction (%v) of AM phase for the three samples are given in Table 1. It shows that the obtained values are slightly higher (2-5%) than expected ones. While the expected value can contain itself an inherit error due to either the fabrication process or the measurement of the volume, the difference is also due to the fact that the voxels at the phases interfaces may belong to more than a single phase due to the partial volume effect (detailed in the “Methods” section). As such, there is always some uncertainty in segmenting the interfacial regions between phases. To evaluate the sensitivity of the uncertainty in this region, from the segmentation results, a dilatation and an erosion of a single pixel layer at the AM phase boundary have been done. This step induces a variation of ±6% on the obtained %v AM. Thus, this discrepancy is considered within the uncertainty range due to the method limitation (*i.e.* image resolution). It is worth noting that the overestimation of %v of AM will lead to the underestimation of the %v of either CBD or pores.

Figure 2a shows the AM phase in MX-1 after being separated into more than 500 individual NMC particles (using Avizo software). It is worth noting that the electrodes studied in this work are for high energy applications, that require high density of AM. This can be seen through the highly packed of NMC particles within the control volume. After the separation of the NMC particles, image-based particle size distribution can be calculated for each sample. Yet, the edge effect of the cropped volume can cause a decrease in particle size. It refers to particles that are at the boundaries of the cropped volume. As such, only a part of them is taken into account for the volume calculation, which under-estimates their exact size. Thus, to better quantify the particle size, all particles touching the volume boundaries have been removed (see Figure S1). Figure 2b shows the particle size distribution of three samples along with the distribution obtained by the laser diffraction measurement on raw material powder. All three sample exhibit the highest peak corresponding to the D_{50} of the materials, despite a slightly lower-than-expected particle size, when comparing to the laser diffraction’s result. Here, we assume that this is due to the calendaring process, which is known to cause fractures of AM particles under the high pressure.[14] This assumption is supported by the visualization of

cracked particles in the SEM image of the MX-2b cross-section in Figure 2d. The cracking parts are also presented in our segmented volume as single AM particles (Figure S1), as we also accounted the internal fissures during the segmentation step. Also, internal pores are observed for NMC secondary particles. Interestingly, we can observe the occasional presence of the CBD inside these internal pores (see purple arrows in Figure 2d), which shows that these pores can be opened to the electrolyte. This observation is in line with the work done by Miller *et al.,*[46] who revealed the penetration of electrolyte through the AM grain boundaries. Thus, the (de)lithiation process can theoretically occur from the inside of the NMC secondary particles, reducing the diffusion length, thereby easing the solid-diffusion process. The broad sphericity distribution (and lower than 1) observed in Figure 2c challenges the assumption on the sphericity of the NMC particles that is made in many simulations.

Image-based approach allows the access to the spatial distribution of the AM particles. Since our sample preparation protocol (see details in 'Methods' section) allows to keep the through-plane direction aligned with the Z-axis during the acquisition step, we can visualize the distribution of the AM particles in the direction normal to the current collector (Figure 2e) (the coordinates of the particle are based on the coordinates of its centroid in space). Our results clearly point out that the big particles tend to move into the bulk of the electrode rather than be in the electrode boundaries (either separator side or current collector side), which is consistent with the work from Ebner *et al.*.[47] For the remaining, most of the particles are well-distributed along the electrode thickness, which can be confirmed with the minor variation of the %v of AM phase with the fraction of total volume in Figure S3. The small particles are found to be more at the boundary of the control volume, which can due to the edge effect mentioned above.

Carbon Binder Domain

The CBD refers to the additives that do not contribute to the capacity of the electrode (inactive materials) but rather to the rate performance of the electrode. It consists of a mixture of good electronically-conducting materials (*e.g.* carbon black, carbon fiber) and a polymeric binder. The CBD provides the mechanical stability of the electrode and establish the electronic conducting pathways within the electrode for most active

materials. Thus, it is expected to be well-percolated and uniformly-distributed throughout the electrode volume. Otherwise, electrons cannot be transported uniformly to all reaction-sites (at the AM particle surface in contact with electrolyte) across the electrode.

Table 2 shows the microstructural properties of the CBD extracted from the 3D microstructure data along with the electronic conductivities measured by the 4 lines method (see Figure S4). Figure 3a shows the 3D CBD distribution and morphology (green) in the three different samples. It can be seen that the CBD tends to form clusters that locate in between neighboring particles rather than a film-like morphology. The presence of CBD clusters observed in this work is consistent with other work [19] [42, 43] based on different approaches. As it is observed in the 2D slices of the Figure 3b, the CBD clusters present a porous morphology, which has been also confirmed by high resolution FIB/SEM data of MX-2b presented in Figure S2, as well as in [19] [42]. Looking at Table 2, the extracted %v of CBD from MX-1 and MX-2b volumes are consistent with the expected values, while in MX-1b, the obtained %v of CBD yields a lower value. Despite a lower %v compared to MX-2b and MX-1b, the CBD network in MX-1 has a larger volume-specific surface area a_{CBD} (Table 2), which refers to the sum of interfacial area CBD/AM, and CBD/pores normalized to the control volume. The decrease of a_{CBD} at higher %v, as it is the case for MX-2b, indicates a more important formation of CBD agglomerates. It is important to note that the formation of CBD agglomerates will negatively impact the inter-connectivity between CBD and the other phases, as it will be discussed later in the paper. The percolation of the CBD is quantified for the three samples (Table 2). As expected, higher %v coupled with a lower a_{CBD} in MX-1b and MX-2b results in a better percolation compared to MX-1.

Figure 3c shows the simulation results of the normalized electronic current density through the control volume in the direction normal to the current collector in the three samples using a diffusion-based method (see details in ‘Methods’ section). It is worth to mention that, the flux density maps include only the pathways that allow moving from one side to the other side of the microstructures, so-called flux-through paths.[48] No or low flux regions were detected by applying an arbitrary threshold value (2% of maximum) to

the flux density map at steady-state, denoted as dead-end paths. They are represented in white in Figure 3b, c.

In MX-1b and MX-2b, a considerable amount of flux-through paths are presented compared to MX-1. These pathways can be considered as long-range connections presented in the CBD network. They are essential for establishing a good inter-connectivity between different regions of the electrode at larger scale, which, along with a better percolation, enhances the electronic conductivity of the electrode.[49]–[51] This hypothesis is supported by the electronic conductivity measurements, shown in Table 2, on the three samples using the four lines method.[52][53] As expected, MX-2b and MX-1b exhibit a higher conductivity along with a lower activation energy compared to MX-1.

While flux-through paths can be considered as long-range contacts that rapidly transport electrons between different regions of the electrode, dead-end paths rather play a role of short-range contacts, which uniformly distribute the electrons to the reaction-sites throughout the electrode. As a result, the synergistic effect which provides both long-range and short-range contacts can be crucial to the electrode performance, especially at high C-rates, as highlighted by several authors.[49]–[51][54]

Pore Network

The pore network is responsible for the ionic transport when filled with the electrolyte. Its microstructure governs the effective ionic conductivity of the electrolyte within the porous structure, which is critical for the electrode performance at high C-rates, especially for high loading electrodes.[55] As expected for high energy density electrodes, the segmentation of the three volumes results in porosities that are unusually low (<20%), as it can be seen in Table 3. Although the porosities are slightly lower than the expected values, they are consistent with the electrode specifications. Despite their low porosities, all three samples exhibit a percolation of the pore network greater than 94%. MX-1b has a lowest porosity but presents a highest volume specific surface area a_{pores}, which is defined in the same way as a_{CBD}. The morphology of the pore network (segmented in blue) in the three different samples is illustrated in Figure 4a.

To investigate the impacts of the pore network on the ionic transport properties, the tortuosity factor and the McMullin number of the pore network are quantified using simulations. However, compared to other microstructural properties such as porosity or volume-specific surface area, the determination of the tortuosity factor is still not standardized in the literature. Our previous work[48] showed that there is a theoretical difference between the tortuosity factors calculated by the two methods: the diffusion-based method (regular method),[56] and the symmetric cell method (SCM).[57][58] The diffusion-based method considers the transport through the porous microstructure whereas the symmetric cell method considers the transport to the AM surfaces within the porous microstructure. As demonstrated in [48], the electrode tortuosity factor, obtained from the SCM, is more suitable to characterize porous electrodes than the commonly-used tortuosity factor. Still, both tortuosity factors are calculated in this work for comparison. Furthermore, the tortuosity factors (in-plane and through-plane) were also quantified allowing the investigation of tortuosity anisotropy. The tortuosity anisotropy has been widely reported in the literature. It has been demonstrated by tomography-based approach as well as experimental measurements (for the case of MCMB active materials) to increase with either the non-spherical AM particles or the calendaring process.[59]–[62] A minor tortuosity anisotropy ($\tau_{\mathrm{through-plane}} > \tau_{\mathrm{in-plane}}$) is reported for NMC electrodes in [61] [62] via simulations using 3D microstructures with numerically-generated CBD. The results can be attributed to the roughly spherical geometry of the raw NMC particle. However, for both methods used for the tortuosity factor determination, the through-plane tortuosity factor is noticed to be significantly lower than the in-plane for all electrodes. Given the low level of porosity ($\varepsilon < 20\%$) studied here, the electrodes might suffer of a high applied pressure during the calendaring step. Thus, it can result in a reduction of the gap between particles in the direction normal to the current collector (Z-axis). The solid phase (NMC particles + CBD) in the three electrodes can, therefore, form agglomerates with their longest axes normal to the current collector. This can prevent the ionic transport in the liquid phase in the direction parallel to the current collector (in-plane), which causes the higher tortuosity in this direction compared to the through-plane direction. To qualitatively verify our hypothesis, we calculated the two-point correlation of the three volumes (two-point correlation analysis is detailed in Supplementary Note 2). The two-

point correlation reveals that the solid phase sizes in the through-plane direction (Z-axis) are significantly larger compared with the in-plane sizes (X and Y-axis) (see Figure S9), as the Z-axis line reach the asymptotic values after the in-plane lines. The through-plane direction should be preferred over the in-plane directions in terms of ionic transport properties in order to improve the electrode performance, since the porous electrode limitations rather develop across the electrode thickness. For the rest of the article, tortuosity will refer to the through-plane tortuosity factor unless otherwise specified.

The results of conventional tortuosity factors (McMullin numbers) show the highest value for MX-1b and the lowest value for MX-2b. Figure 4b shows the simulation results using the diffusion-based method, in which we can see the flux density passing through the three volumes (via flux-through pores). The flux density map reveals a uniform distribution of flux for MX-1. In contrast, MX-1b and MX-2b both show locally higher flux density regions pointing out to a heterogeneous flux-through porosity. The high flux density regions may represent the restriction/constriction effects (bottlenecks) in the pore network, which may be useful for understanding localized degradation mechanisms. Besides, the simulation of diffusion flux passing through the volumes allows the identification of the flux-through and dead-end pores, as can be observed in Figure 4c.

Using the SCM, we can see a decreasing trend of the electrode tortuosity factors and McMullin numbers compared to the previous values for all electrodes in all directions (Table 3). The MX-1b still has the most tortuous pore network compared to the other two in terms of electrode tortuosity factor. In both approaches, the lowest tortuosity factor is found for MX-2b, even though it does not have the highest porosity. Although the differences between two methods are not apparent, it is worth to restate that the SCM relies on the (dis)charging of double-layer capacitance at the solid/liquid interface throughout the electrode instead of the diffusional flux through the porous structure as for diffusion-based method. Thus, it takes into account both flux-through and dead-end pores contributions to the overall ionic transport of the pore network.[48] In Figure 4c, the dead-end pores presented in the ortho-slices (colored in white) are mainly small sections and disconnected (%v < 5% and without percolation), which results in slight effects on the tortuosity of the pore networks when the SCM is considered.[48]

Inter-connectivity between phases

The inter-connectivity between the different phases within the electrode is investigated in the following section, as it constitutes an important parameter for the electrode to achieve a good electrochemical performance. For this purpose, we adopted a statistical approach in which more than 500 individual particles within each volume were separately studied. It is worth noting that, in this section, all the volume-specific interfacial areas and the triple-phase boundary (TPB) density, *i.e.* the boundary where the three different phases (AM, CBD, pores) meet, are normalized by each AM particle volume and not by the control volume as in the previous sections. The subscript p is added to these metrics (a_p, TBP_p density) to avoid confusion.

For fuel cell electrodes, TPB is the exact location that electrochemical reactions take place during the operation, since it is the meeting point of three components that are required for the electrochemical process. In contrast, for lithium-ion battery, the electrochemical reactions are not necessary take place unique at the TPB but rather at the AM/electrolyte interface, as will be discussed later in the text. Yet, the TPB for lithium-ion battery remains the reaction-site that costs a lowest polarization related to the electrochemical reaction.

Figure 5a shows the distribution of the interfacial area between the AM particles and the CBD of the three samples, $a_{P(AM/CBD)}$. MX-2b has the highest inter-connectivity between NMC and CBD among the samples along with a large dispersion. Despite a lower %v of CBD, MX-1 possesses a lower dispersion of $a_{P(AM/CBD),}$ which represents a more uniform distribution of the CBD. However, the lower average interfacial area with CBD found in MX-1 might introduce an additional contact resistance due to the poor AM particle-CBD contacts.

The interfacial area between the AM and the pores, $a_{P(AM/pores)}$, is also determined and shown in Figure 5a. This interfacial area corresponds to the electrochemical active surface area, where the charge transfer process occurs. It is worth noting that although the CBD can eventually be ionically-conducting by considering either the ability to absorb electrolyte the PVdF[63]–[65] or the porous morphology showed above, one might expect it

to have lower ionic transport properties at high C-rates than the electrolyte filling in the pores. The presence of CBD at the AM surface can, therefore, negatively impact the kinetics of charge transfer at the interface AM/CBD. Hence, the interfacial area between AM/pores will mainly determine the exchange current density (A/m^2_{ASA}) within the porous electrode. Consequently, assuming all the AM surface are in contact with electrolyte only (*i.e.* ignoring the CB coverage of the AM particles) can potentially lead to errors in the evaluation of electrode properties used for the simulation of the electrode behavior.[12] MX-1 yields a higher AM/pores interfacial area compared to MX-1b and MX-2b, which can be explained by its highest porosity and its lower AM/CBD interfacial area.

Figure 5b shows the distribution of TPB_p density at each particle in the three samples. The TPB_p density per particle volume was found to be the highest in the sample MX-2b, in average. This sample also presents the largest dispersion of the TPB_p density values. In contrast, sample MX-1 presents a lower average for the TPB_p density values but with a more uniform distribution. The results from $a_{P(AM/CBD)}$ and TPB_p density unveil the impact of %v of CBD on the three microstructures considered in this study. Even though the CBDs in MX-1b and MX-2b have a smaller volume-specific surface area (a_{CBD}) than in MX-1, both are still able to provide a larger interfacial area $a_{P(AM/CBD)}$ and a higher TPBs density throughout the microstructures due to a higher amount of CBD. This means that the CBD is still well-dispersed throughout the volume in the samples with high %v of CBD that have been used in this work. The mechanism of lacking short-range contacts for a higher %v CBD, as mentioned above, is therefore not valid for samples MX-1b and MX-2b. This can be confirmed further with the visualization of the CBD in Figure 3a, in which one can see that the CBD distributes well over the entire volume of MX-1b and MX-2b (very few spaces without the CBD).

Figure 5c, e, f show the percentage of particles surface covered by the CBD and the pores by particles for MX-1b, MX-2b and MX-1 respectively. The TPB_p density of each particle is also represented with a color scale bar. A broader distribution can be seen for the MX-2b and MX-1b as discussed previously. Furthermore, smaller particles tend to have a higher cover ratio of CBD as well as TPB_p density. On the other hand, larger particles show a higher cover ratio of pores. A “representative” particle having an effective %s.

covered by CBD (~14%) and pores (~56%) is showed for sample MX-1 in Figure 5d along with its TPB_p map. This particle can be relevant for macroscopic modelling approach.

In summary, the sample MX-1 shows a higher degree of uniformity than MX-1b and MX-2b in terms of inter-connectivity between phases at particle scale. As a result, one might expect lower microstructural heterogeneities effects during operation for MX-1 compared to the others, which can be detrimental for the performance. This is in line with what has been reported by Müller *et al.*[21] and Forouzan *et al.*[23] through numerical modeling.

The figure 6a displays the results of the rate capability of the three electrodes measured in a coin-cell setup at 25°C (see Methods section). The rate capability allows assess the performance of an electrode under different currents density. It shows that MX-1 outperforms the MX-1b (same loading), especially at high current density region (I>I*), whereas MX-1b presents a higher TPB_p density and a higher %v of CBD. It is worth mentioning that MX-2b also underperforms when comparing to an electrode having the same loading with lower %v of CBD (this electrode, however, is not studied in this work). It is worth noting that for the battery porous electrodes such as graphite or some oxide materials, the charge transfer does not occur only at the TPB_p, since the AM phase can have an appreciable electronic conductivity. For NMC material, this is particularly true once it is partially delithiated.[66] Thus, the lack of AM/CBD interfacial area, as well as a low TPB_p density, can be compensated by the electronic transport through the NMC particles to join the reaction-sites, as discussed in [11] [45]. In addition, the brutal drop of the rate capability in the high current density region is commonly attributed to the porous electrode effects, *i.e.* through the McMullin number as the main limitation is considered to be in the liquid phase. Nevertheless, by using a 3D particle-resolved, mesoscale model to investigate the electrochemical behaviors on a per-particle and per-surface basis, Ferraro *et al.*[45] demonstrated a significant capacity loss coming from the reaction rate at the surface of AM particles. The latter is directly related to both interfacial surface area: AM/Pores and AM/CBD of each particle. In light with this, based on the analysis results in our work (Figure 5), the excess of CBD (MX-1b, MX-2b) might cause an additional issue for the electrode performance at high C-rates. Indeed, it can lead to the reduction of electrochemical active surface area at the particle scale, due to the ionically-blocking

properties of the interface AM/CBD, as illustrated in Figure 6b. This consequence of the CBD excess has been reported by several authors.[12][13][38][40][45] Consequently, the solid-diffusion limitation can be exacerbated due to the lower electrochemical surface area, because of longer diffusive pathways for lithium to travel from the surface to the bulk of the NMC particles. This results in an underutilization of AM. However, this scenario is only valid when the AM has a good electronic conductivity, which can compensate for the lack of the AM/CBD interface and/or the TPB_p density, as discussed above. For an AM with high electronic resistance, the TPB_p density can be vital for the performance of the electrode at high C-rates, as reaction-sites mainly sit at the TPB. For instance, since NMC exhibits a reduction of electronic conductivity at the vicinity of the full lithiation state, Ferraro *et al.*[45] observed a higher reactivity at the interfacial area between AM and porous CBD (*i.e.,* there is electrolyte within the pores of CBD), which consists of multi TPB_p. Here, as NMC exhibits a good electronic conductivity,[66] the performance at high C-rate seems to be negatively impacted by the excess of CBD, as observed for MX-1b and MX-2b. Thus, to improve the power rate of the Li-ion battery electrodes having a good electronic conductivity AM, one should go for high values of interfacial area between AM and pores rather than between AM and CBD. A porous CBD phase can also create positive impacts as it allow the electrolyte to impregnate, so that increases the AM/Pore interface.

Besides, microstructural heterogeneities can also significantly impact the electrode performance. Here, a higher degree of uniformity observed in MX-1 compared to MX-1b could help minimize the electrochemical heterogeneities, improve material utilization, and reduce polarization losses during operation. All result in a better rate capability.

Conclusion

In this work, we demonstrated that the X-ray holotomography-based approach is an efficient way to reveal valuable insights about the microstructural properties and the electrode heterogeneity that is not straightforward to quantify using regular electrochemical-based approaches.

We show that with higher %v of CBD, the CBD provides a higher interfacial area with the AM phase, along with the tendency to form agglomerates. The formation of agglomerates promotes the formation of long-range contacts within the porous electrode, which provides a good electronic conductivity. However, electrode performance is observed to be deteriorated at high C-rates, with higher %v of CBD, when comparing two electrodes with the same loading but with different ratios. Based on the analysis, we suggested herein that increase the %v of CBD causes a decrease of the electrochemical active surface area (surface area AM/pores). For an electronically-conducting AM, the TPB density and the AM/CBD interfacial area are thought to have minor effects on the performance at high C-rates. Thus, to improve the power rate of the Li-ion battery high-energy electrodes, engineering of electrode design should aim for high values of interfacial area between AM/pores instead. Also, the research for an “ideal” CBD morphology needs to consider simultaneously different aspects and not only the electrical conductivity, *i.e.* simply increase the %v of CBD would not be an obvious solution to improve the overall performance.

Regarding the pore network, we compared the two methods for tortuosity factor determination: the diffusion-based method (regular tortuosity factor) and the SCM (electrode tortuosity factor). A decrease trend was observed when comparing the electrode tortuosity factor to the regular tortuosity factor, which highlights a positive contribution of the dead-end pores to the overall ionic transport, albeit it is small compared to that of through pores, at least with the electrodes studied here. The tortuosity anisotropy of the pore network has been observed for through-plane and in-plane directions for both methods. The tortuosity factor in the direction normal to the current collector was found to be substantially lower than the in-plane direction (about half). Although the cause of the anisotropy stays uncertain, a hypothesis that is related to the calendaring process used in this work to achieve electrodes with a high energy density was proposed.

Finally, a higher heterogeneity in terms of inter-connectivity between phases at particle scale was also found for the electrodes with higher %v of CBD, which can lead to higher risk of performance deterioration during battery operation. All of these results are to be

included in a numerical model to a quantitative investigation of their effects on the performance in a follow-up study.

Methods

Analyzed samples

Three different positive electrodes are investigated in this work and labelled as MX-1, MX-1b, MX-2b. Each electrode is a mixture of $LiNi_{0.5}Mn_{0.3}Co_{0.2}O_2$, conductive carbon black and polyvinylidene fluoride (PVdF) with different composition. Their specifications are shown in Table 1, 2 and 3, where expected values of AM, CBD and pores are reported respectively.

The particle size distribution of the raw $LiNi_{0.5}Mn_{0.3}Co_{0.2}O_2$ particles is determined with the laser diffraction method. This method is a widely used particle sizing technique for materials ranging from hundreds of nanometers up to several millimeters in size. It measures particle size distribution by measuring the angular variation in intensity of light scattered as a laser beam passes through a dispersed particulate sample. Large particles scatter light at small angles relative to the laser beam and small particles scatter light at large angles. The angular scattering intensity data is then analyzed to calculate the size of the particles responsible for creating the scattering pattern, using the Mie theory of light scattering. The particle size is reported as a volume equivalent sphere diameter. As for output, laser diffraction will give a volume-weighted distribution. That is, the contribution of each particle in the distribution relates to the volume of that particle, *i.e.,* the relative contribution will be proportional to size.

Sample preparation

The sample preparation is a crucial step to get a high-quality result and to avoid artefacts during the acquisition process. Then, a careful preparation of the sample is needed to have the sample size required for X-ray nano-tomography. When performing X-ray tomography, the size of the sample is of importance. The first obvious reason is linked to the absorption of the X-rays. Indeed, because it is a transmission technique, it is necessary to have enough X-rays going out of the sample to have enough signal on the detector. The second reason is linked to the field of view of the detector. The 3D resolution will be better if the sample lateral size fits into this field of view. Local X-ray tomography, *i.e.* into samples that are bigger than the field of view, are possible but usually results in a compromise on the final resolution. As the field of view is equal to the number of pixel on the camera times the pixel size, it is usually quite large for micro-scale X-ray tomography. Then, appropriate sizing of ex-situ samples (from 0.5 to few mm) is typically not a problem. In this study the pixel size used was 50nm and corresponds to a field of view of 130 µm. Moreover, because of the absorption of the NMC particles at the used energy, an optimal size of 50 µm diameter has been calculated.

For this, a “free-standing” electrode was first required, which was typically obtained by simply peeling the porous electrode material off the current collector foil. A laser cutter built in-house at IMPMC laboratory was used to precisely cut a pillar of *ca.* 50 µm in diameter from the bulk electrode. It is worth mentioning that to avoid any damage of the laser beam on the region of interest, the pulse mode was used for laser beam instead of permanent mode. Then, the electrode pillar was mounted on the tip of a quartz capillary, which is mounted on the sample holder, using cyanoacrylate glue (see Figure S5).

Electrochemical measurements

All measurements are carried out in a controlled temperature chamber at 25°C. The cycling test were performed with a multipotentiostat (Biologic, France). The operational range for the NMC materials in this work is chosen between 2.5 and 4.3 V versus Li/Li^+.

All coin cells first undergo a formation process in which they are cycled four times with constant-current (CC) discharge/charge cycles at C/10 to form a stable passive layer the particle surface. For the fifth cycle, a constant voltage (CV) is held at the end of the discharge until the current gets down to C/50. This extra steps before further charging were to ensure that the electrode completely lithiated (pristine state) after removing all possible limitations (for example: solid-diffusion limitation). Finally, a CCCV charge followed by a CC discharge are carried out, both at C/25, for capacity determination. The available capacity is determined at the end of the CC discharge.

Rate-capability tests are performed on either a VMP3 or a BCS (Bio-Logic, France). The rate experiments were conducted on two separate electrodes of the same composition for the reproducibility. We assume that there is no electrode degradation during the measurements. The cells are cycled with different currents following by a CV at the end of each cycle to reach a stable stoichiometry until the current gets lower than C/50. In the rate capability test, the cells were charged with a CC phase followed by a CV phase, which remained unaltered, independent of the applied discharge current. Between each charge and discharge cycle a pause of 1 h was kept to allow for relaxation of the cells. In the discharge procedure, the cells were discharged with C/25, C/10, C/5, C/2, 1C, 2C.

For effective electronic conductivity determination, Electrochemical Impedance Spectroscopy (EIS) were carried out using ITS system with the 4 lines configuration, and MTZ device from Biologic, France. The 4 lines configuration (see the experiment setup in Figure S3) is known to minimize the impact from the contact resistances between the probes and the sample, which can vary along with the applied pressure on the sample. The temperature was set to vary within a range [-20°C,60°C] allowing to extract the activation energy of the electronic conductivity. Activation energy close to zero refers to a metallic behavior of the materials, which provides good electronic conducting pathways.

Holographic X-ray nanoCT technique for Li-ion battery

The interaction of X-rays with a material may be described through the index of refraction n, such as : $n = 1 - \delta - i\beta$. β is the absorption coefficient and δ is the decrement of the refractive index and refer ,respectively, to the change of amplitude and the phase shift of the X-ray, as it passing through the materials.

The holotomography technique used in this study and developed by Cloetens *et al.*[33] is based on phase contrast imaging. It gives high contrast images for low atomic number samples. The setup at the ID16B beamline of the European Synchrotron Radiation Facility (ESRF)[67] is described in figure1a. The high flux ($8X10^{10}$) nano-beam ($50x50nm^2$) is used as a secondary source. Thanks to the diverging beam of 29.6keV, four tomographies at four different distances from the focal plane are performed by acquiring 2515 projections over 360° with an exposure time of 0.4s per 2D image recorded on a PCO edge 5.5 camera. The 3D reconstructions with a pixel size of 50 nm are achieved in two steps: (1) recursive phase retrieval calculation[68][69] using an in-house developed octave script based on a Paganin-like[70] approach with a delta/beta of 137 and (2) filtered back projection reconstruction using ESRF software PyHST2.[71]

Data processing

Pre-processing

Due to shortcomings in the image acquisition process, the base signal of an X-ray scan is often superimposed by different kind of image artefacts, that can be observed in the reconstructed image most frequently as noise, and blur effects.[72][73] For multi-phases microstructures, these effects can be very disturbed for the segmentation step. Therefore, pre-processing of the reconstructed 2D images might be needed to improve the image quality, allowing a good result in the segmentation process.[72][73]

In this work, we applied a non-local mean filter subsequently following by an unsharp mask for edge enhancement systematically to all the tomographic data. Non-local means filter has been reported to be an excellent candidate to efficiently remove noise and at the same time conserve edges between objects. In addition, an unsharp mask is for edge enhancement after denoising process. It reduces the partial volume effect (see Supplementary Note 1) due to image blur and/or low resolution. As it can be seen in Figure S6, the contrast between the CBD and the pore space was enhanced after filtering. Figure S8 illustrates the partial volume effect, when the boundaries between two phases do not manifest themselves as crisp intensity steps (type Dirac signal), but rather as gradual grey level changes spanning several voxels. The contrasts between phases are improved while preventing details loss, as shown in the histogram (global) and line profile (local) of the image (Figure S6).

Pietsch *et al.*[22] have reported that the uncertainty of the segmented data is well correlated with the Otsu inter-class variance. Here, we evaluated this metric on our dataset before and after the filtering process. The filtering process allows to get a better inter-class variance, hence reduces the uncertainty of the segmentation process.

Image segmentation

Image segmentation is a crucial step in image processing and affects all subsequent image analyses. It is commonly done by histogram evaluation, which considers only voxel's grey level (global thresholding). This approach can be very efficient in terms of computational time and efforts if high contrast between phases is presented, *i.e.* separate peaks appear in the histogram. However, for a multi-phases microstructure, each phase is frequently represented by a distribution of grey level that can be partially overlapped with others, or even completely hidden in the histogram. Hence, the threshold uncertainty range can be significant when using a global approach. Moreover, it is worth to note that since this approach is based only on voxel's grey level, it can be susceptible to the partial volume effect. Local segmentation methods such as watershed, converging active contours, show a better performance on the multiphase segmentation of tomographic images, as reported by Schlüter *et al.*.[72] However, they always rely on grey's level and/or gradient of grey values of pixels for the classification.

In this work, the segmentation was performed with an ImageJ's plugin named Weka,[74] which involved machine learning in performing the segmentation. This approach is based on features extracted from the image through a set of different filters. It is based on microstructural information captured from the image (2D) or volume (3D) to train a machine learning model rather than the only grey level for the classification of voxels. The model uses a random forest algorithm, which has been reported to be relevant for classification task without the need for substantial computational resources. This tool is part of the machine learning field, so-called "supervised learning", that needs a label data to train the model. Regarding the label data, the users have to carefully classify the pixels (taken from different slices located throughout the volume depth) into different classes (three in this work) based on various criteria: the pixel's grey value, the pixel's neighborhood, the morphology of each phase (e.g., the AM particle frequently takes a roughly spherical geometry, while the CBD tends to form clusters in between AM particles). The pixels that were classified by the users are then considered as "reference label". They are used for the training step to get the best model that minimizes the errors. The model is applied to segment the rest of the volume automatically. We repeat this process for each sample in this work. The label data, therefore, needs to be carefully selected by users. The labelling step is mainly based on the subjective human opinion about the difference of grey value and can vary upon people. Thus, having a pre-processing step to improve the quality of the image can be helpful to reduce the segmentation error. We compared the segmentation results of the AM phase in MX-2b with the segmentation result of the same phase using binary threshold technique on the high resolution FIB/SEM data to validate our segmentation. (Figure S7).

Microstructural analysis

Once images are segmented into three separated phases, the reconstructed 3D volumes of the electrodes were imported into the commercial software package Avizo V9.4 (Avizo, Thermo Fisher Scientific, Waltham, Massachusetts, USA) for 3D visualization and NMC particles separation. The particle size distribution is used as reference to adjust parameters of the separation object algorithm in Avizo.

The phase volume fraction is defined by the ratio: $\frac{V_i}{V}$, where V_i refers to the volume of phase *i*, calculated as the percentage of voxels corresponding to this phase, and V to the total volume of the control volume.

The percolation represents the intra-connectivity of the phase *i*. It is quantified by the ratio between all connected voxels of phase *i* to the total voxels of this phase (connected and isolated voxels) within the control volume. Voxels that share a common face are considered as connected.

The sphericity is a measure of how closely the shape of an object resembles that of a perfect sphere. It is defined by the ratio of the surface area of a sphere with the same volume as the given particle to the surface area of the particle: $\psi_p = \frac{\pi^{\frac{1}{3}} V_p^{\frac{2}{3}}}{A_p}$, where ψ_p, V_p and A_p are the sphericity, the volume and the surface area of the individual particle respectively. The sphericity is calculated for each individual AM particle.

The specific surface area quantifies the surface area of phase *i* per unit electrode volume. On the other hand, the specific interfacial surface area refers to the total surface area of the interface between two phases *i*, *j* per unit electrode volume.

It is worth to note that our analysis is based on voxelized data for convenience such that a meshing process is not necessary. This approach is relevant for volume quantification as it shows comparable results to other approaches. However, for surface area, this approach tends to overestimate the value of the surface area, even though with a high value of resolution. The marching cube (MC) algorithm[75] is shown to give the highest accuracy for the surface area calculation.[30] This algorithm polishes the originally derived voxel-based surface mesh as described in [75]. The ratio a_{voxel} , a_{MC} of the three volumes analyzed here varies from 1.2 to 1.3. Nevertheless, we may have of particular interest to the relative values rather than the absolute one since the comparison between samples can still give us insight about the effects of microstructures.

The TPB density is defined as the length of the intersection among three phases *i*, *j*, and *k*, normalized by the total volume of the microstructure domain. For voxelized data used in this work, a TPB is defined as the length of the edges where three of the four connecting voxels contain different phases.

Most of the parameters studied throughout this work are straightforward to quantify using either *TauFactor* and/or built-in tools or plugins in Fiji or Avizo. The visualization of the TPBs required adding work.[76] *TauFactor* is an open-source MATLAB application developed by Cooper *et al.*[77] allowing a complete characterization of the microstructure based on image data. The analysis were proceeded first on separated phases (AM, CBD, pores), then on the correlation between phases to capture the microstructural characteristics of the electrodes as a whole. Furthermore, based on the *TauFactor* framework, an in-house code was developed. It allows extracting different microstructural properties when the AM phase was separated into individual particles.

For tortuosity factor determination, our previous work in [48] unambiguously demonstrated that the electrode tortuosity factor given by the symmetric cell method is a more appropriate metric to characterize porous electrodes than the conventional tortuosity factor determined with the diffusion-based method. Hence, in this work, we quantified both tortuosity factors using two approaches for comparison.

Recently, Gayon-Lombardo *et al.*[78] proposed to use periodic boundaries instead of Dirichlet boundaries for the diffusion-based method for the conventional tortuosity factor determination. They suggested that this approach allows representing better the bulk behavior of the microstructure. Thus, it might be interesting for future works to evaluate the electrode tortuosity factor under the same conditions and to compare the two methods as what has been done by Nguyen *et al.*.[48]

To study the morphology of the CBD, the diffusion-based method was also used for the simulation of a flux of electrons passing through the control volume via the CBD. Although this simulation relies on the Fick's law, the governing equation is mathematically homologue to the Ohm's law, which governs the electronic transport in CBD.

Despite the large acquisition volume given by the X-ray holotomography technique, there is one sample that suffered from crack, which reduces significantly the exploitable data. Consequently, to be consistent in the comparison, we considered an adequate sub-volume of 25x25x25 μm^3 in each of the three samples and defined as the control volume. In addition, a representative volume analysis had been done to study the representativeness of this control volume. As can be seen in Figure S3, all three volumes can be considered as homogeneous and representative. The two-point correlation calculation also showed in Figure S9 that the asymptotic behavior is reached for all the three volumes justifying the representativeness of the control volume.

Acknowledgements

The authors would like to acknowledge French National Association for Research and Technology (ANRT) for partially supporting the funding of this research work. T-T.N was supported by Renault Group for his PhD Project. Authors would like to thank Yoann Guarnelli (IMPMC, Paris, France) for the help with the laser cutter used for sample preparation in this work, and Imène Estève (IMPMC, Paris, France) for the FIB/SEM images. The authors also acknowledge the European Synchrotron Radiation Facility for provision of beam time (in-house research time) using the ID16B beamline.

Conflict of Interest

The authors declare no conflict of interest.

Author Contributions

T-T.N prepared the samples for the imaging campaign. J.V and R.T performed the X-ray nano-holotomographic experiments. T-T.N and B.F performed the electronic conductivity measurements. T-T.N and Z.S studied the image processing methodology. T-T.N wrote the manuscript. All authors contributed to scientific discussions and the revision of the paper. The work is supervised by B.D, B.F, A.D. and C.D.

References

[1] J.B. Goodenough, *J. Solid State Electrochem.* **2012**, *16*, 2019.

[2] J.-M. Tarascon, *Trans. R. Soc. A* **2010**, *368*, 3227.

[3] J.B. Goodenough, Y. Kim, *Chem. Mater.* **2010**, *22*, 587.

[4] J.B. Goodenough, *Energy Environ. Sci.* **2014**, *7*, 14.

[5] X. Zhang, Z. Ju, Y. Zhu, K.J. Takeuchi, E.S. Takeuchi, A.C. Marschilok, G. Yu, *Adv. Energy Mater.* **2020**, 2000808.

[6] F. Pouraghajan, H. Knight, M. Wray, B. Mazzeo, R. Subbaraman, J. Christensen, D. Wheeler, *J. Electrochem. Soc.* **2018**, *165*, 2644.

[7] D.E. Stephenson, B.C. Walker, C.B. Skelton, E.P. Gorzkowski, D.J. Rowenhorst, D.R. Wheeler, *J. Electrochem. Soc.* **2011**, *158*, A781.

[8] J.E. Vogel, M.M. Forouzan, E.E. Hardy, S.T. Crawford, D.R. Wheeler, B.A. Mazzeo, *Electrochim. Acta* **2018**, *297*, 820.

[9] S. Wen Peterson, S. Wen, **2015**.

[10] J. Landesfeind, M. Ebner, A. Eldiven, V. Wood, H.A. Gasteiger, *J. Electrochem. Soc.* **2018**, *165*, A469.

[11] B.L. and E.M. F. Cadiou, T. Douillard, N. Besnard, **n.d.**

[12] L. Almar, J. Joos, A. Weber, E. Ivers-Tiffée, *J. Power Sources* **2019**, *427*, 1.

[13] H. Zheng, L. Tan, G. Liu, X. Song, V.S. Battaglia, *J. Power Sources* **2012**, *208*, 52.

[14] R. Xu, Y. Yang, F. Yin, P. Liu, P. Cloetens, Y. Liu, F. Lin, K. Zhao, *J. Mech. Phys. Solids* **2019**, *129*, 160.

[15] P. Pietsch, V. Wood, *Annu. Rev. Mater. Res.* **2017**, *47*, 451.

[16] V. Wood, *Nat. Rev. Mater.* **2018**, *3*, 293.

[17] C. Cao, M.F. Toney, T.-K. Sham, R. Harder, P.R. Shearing, X. Xiao, J. Wang, *Mater. Today* **2019**.

[18] D.S. Eastwood, R.S. Bradley, F. Tariq, S.J. Cooper, O.O. Taiwo, J. Gelb, A. Merkle, D.J.L. Brett, N.P. Brandon, P.J. Withers, P.D. Lee, P.R. Shearing, *Nucl. Instruments Methods Phys. Res. Sect. B Beam Interact. with Mater. Atoms* **2014**, *324*, 118.

[19] S.R. Daemi, C. Tan, T. Volkenandt, S.J. Cooper, A. Palacios-Padros, J. Cookson, D.J.L. Brett, P.R. Shearing, **2018**.

[20] S.J. Cooper, D.S. Eastwood, J. Gelb, G. Damblanc, D.J.L. Brett, R.S. Bradley, P.J. Withers, P.D. Lee, A.J. Marquis, N.P. Brandon, P.R. Shearing, *J. Power Sources* **2014**, *247*, 1033.

[21] J. Eller, M. Ebner, C. Burns, J. Dahn, V. Wood, *J. Electrochem. Soc.* **2018**, *165*, 339.

[22] P. Pietsch, M. Ebner, F. Marone, M. Stampanoni, V. Wood, *Sustain. Energy Fuels* **2018**, *2*, 598.

[23] M.M. Forouzan, B.A. Mazzeo, D.R. Wheeler, *J. Electrochem. Soc.* **2018**, *165*.

[24] D. Kehrwald, P.R. Shearing, N.P. Brandon, P.K. Sinha, S.J. Harris, *J. Electrochem. Soc.* **2011**, *158*, A1393.

[25] S.J. Harris, P. Lu, *J. Phys. Chem. C* **2013**, *117*, 6481.

[26] M. Kerlau, M. Marcinek, V. Srinivasan, R.M. Kostecki, *Electrochim. Acta* **2007**, *52*,

5422.

[27] Y. Yang, R. Xu, K. Zhang, S. Lee, L. Mu, P. Liu, C.K. Waters, S. Spence, Z. Xu, C. Wei, D.J. Kautz, Q. Yuan, Y. Dong, Y. Yu, X. Xiao, H. Lee, P. Pianetta, P. Cloetens, J. Lee, K. Zhao, F. Lin, Y. Liu, *Adv. Energy Mater.* **2019**, *9*, 1900674.

[28] T. Hutzenlaub, A. Asthana, J. Becker, D.R. Wheeler, R. Zengerle, S. Thiele, *Electrochem. Commun.* **2013**, *27*, 77.

[29] L. Zielke, T. Hutzenlaub, D.R. Wheeler, C.-W. Chao, I. Manke, A. Hilger, N. Paust, R. Zengerle, S. Thiele, *Adv. Energy Mater.* **2015**, *5*, 1401612.

[30] J. Joos, T. Carraro, M. Ender, B. Rüger, A. Weber, E. Ivers-Tiffée, **n.d.**

[31] P.R. Shearing, D.S. Eastwood, R.S. Bradley, J. Gelb, S.J. Cooper, F. Tariq, D.J.L. Brett, N.P. Brandon, P.J. Withers, P.D. Lee, *Exploring Electrochemical Devices Using X-Ray Microscopy: 3D Micro-Structure of Batteries and Fuel Cells*, **n.d.**

[32] V. Julie, L. Jérôme, C. Peter, B. Pierre, D. Gérard, S. Heikki, U.V. François, *J. Power Sources* **2013**, *243*, 841.

[33] P. Cloetens, W. Ludwig, J. Baruchel, D. Van Dyck, J. Van Landuyt, J.P. Guigay, M. Schlenker, *Cit. Appl. Phys. Lett* **1999**, *75*, 5486.

[34] Z. Su, V. De Andrade, S. Cretu, Y. Yin, M.J. Wojcik, A.A. Franco, A. Demortière, *ACS Appl. Energy Mater.* **2020**, acsaem.9b02236.

[35] D.P. Finegan, M. Scheel, J.B. Robinson, B. Tjaden, I. Hunt, T.J. Mason, J. Millichamp, M. Di Michiel, G.J. Offer, G. Hinds, D.J.L. Brett, P.R. Shearing, *Nat. Commun.* **2015**, *6*, 1.

[36] V. Vanpeene, J. Villanova, J.P. Suuronen, A. King, A. Bonnin, J. Adrien, E. Maire, L. Roué, *Nano Energy* **2020**, *74*, 104848.

[37] M. Chouchane, A. Rucci, T. Lombardo, A.C. Ngandjong, A.A. Franco, *J. Power Sources* **2019**, *444*, 227285.

[38] A.N. Mistry, K. Smith, P.P. Mukherjee, **2018**.

[39] G. Inoue, M. Kawase, *J. Power Sources* **2017**, *342*, 476.

[40] M.E.F. Bradley L. Trembacki, Aashutosh N. Mistry, David R. Noble, and S.A.R. Partha P. Mukherjee, *J. OfThe Electrochem. Soc.* **2018**, *165*, E725.

[41] X. Lu, A. Bertei, D.P. Finegan, C. Tan, S.R. Daemi, J.S. Weaving, K.B.O. Regan, T.M.M. Heenan, G. Hinds, E. Kendrick, D.J.L. Brett, P.R. Shearing, *Nat. Commun.* **2020**, *11*, 1.

[42] S. Müller, M. Lippuner, M. Verezhak, V. De Andrade, F. De Carlo, V. Wood, *Adv. Energy Mater.* **2020**, 1904119.

[43] S.L. Morelly, J. Gelb, F. Iacoviello, P.R. Shearing, S.J. Harris, N.J. Alvarez, M.H. Tang, **2020**, *7*, 32.

[44] O.O. Taiwo, D.P. Finegan, J. Gelb, C. Holzner, D.J.L. Brett, P.R. Shearing, *Chem. Eng. Sci.* **2016**, *154*, 27.

[45] M.E. Ferraro, B.L. Trembacki, V.E. Brunini, D.R. Noble, S.A. Roberts, *J. Electrochem. Soc.* **2020**, *167*, 013543.

[46] D.J. Miller, C. Proff, J.G. Wen, D.P. Abraham, J. Bareño, *Adv. Energy Mater.* **2013**, *3*, 1098.

[47] M. Ebner, F. Geldmacher, F. Marone, M. Stampanoni, V. Wood, *Adv. Energy Mater.* **2013**, *3*, 845.

[48] T.T. Nguyen, A. Demortière, B. Fleutot, B. Delobel, C. Delacourt, S.J. Cooper, *Npj Comput. Mater.* **2020**, *6*, 1.

[49] S.L. Morelly, N.J. Alvarez, M.H. Tang, *J. Power Sources* **2018**, *387*, 49.

[50] H. Bockholt, M. Indrikova, A. Netz, F. Golks, A. Kwade, *J. Power Sources* **2016**, *325*, 140.

[51] R. Tang, Q. Yun, W. Lv, Y.B. He, C. You, F. Su, L. Ke, B. Li, F. Kang, Q.H. Yang, *Carbon N. Y.* **2016**, *103*, 356.

[52] B.J. Lanterman, A.A. Riet, N.S. Gates, J.D. Flygare, A.D. Cutler, J.E. Vogel, D.R.

Wheeler, B.A. Mazzeo, *J. Electrochem. Soc.* **2015**, *162*, 2145.

[53] S.W. Peterson, D.R. Wheeler, *J. Electrochem. Soc.* **2014**, *161*, A2175.

[54] Y. Shi, L. Wen, S. Pei, M. Wu, F. Li, *J. Energy Chem.* **2019**, 19.

[55] S. Malifarge, B. Delobel, C. Delacourt, *J. Electrochem. Soc.* **2018**, *165*, A1275.

[56] I. V. Thorat, D.E. Stephenson, N.A. Zacharias, K. Zaghib, J.N. Harb, D.R. Wheeler, *J. Power Sources* **2009**, *188*, 592.

[57] S. Malifarge, B. Delobel, C. Delacourt, *J. Electrochem. Soc.* **2017**, *164*, E3329.

[58] J. Landesfeind, J. Hattendorff, A. Ehrl, W.A. Wall, H.A. Gasteiger, *J. Electrochem. Soc.* **2016**, *163*, A1373.

[59] M. Ebner, D.W. Chung, R.E. García, V. Wood, *Adv. Energy Mater.* **2014**, *4*.

[60] B. Suthar, J. Landesfeind, A. Eldiven, H.A. Gasteiger, *J. Electrochem. Soc.* **2018**, *165*, 2008.

[61] B.L. Trembacki, D.R. Noble, M.E. Ferraro, S.A. Roberts, *J. Electrochem. Energy Convers. Storage* **2020**.

[62] K.S. F.L.E. Usseglio-Viretta, A. Colclasure, A.N. Mistry, K.P.Y. Claver, F. Pouraghajan, D.P. Finegan, T.M.M. Heenan, D. Abraham, P.P. Mukherjee, D. Wheeler, P. Shearing, S.J. Cooper, *J. Electrochem. Soc.* **2018**, *165*, A3403.

[63] G. Liu, H. Zheng, S. Kim, Y. Deng, A.M. Minor, X. Song, V.S. Battaglia, *J. Electrochem. Soc.* **2008**, *155*, A887.

[64] M. Doyle, J. Newman, A.S. Gozdz, C.N. Schmutz, J. Tarascon, *J. Electrochem. Soc.* **1996**, *143*, 1890.

[65] J. Li, L. Christensen, M.N. Obrovac, K.C. Hewitt, J.R. Dahn, *J. Electrochem. Soc.* **2008**, *155*, A234.

[66] R. Amin, Y.-M. Chiang, *J. Electrochem. Soc.* **2016**, *163*, A1512.

[67] G. Martinez-Criado, J. Villanova, R. Tucoulou, D. Salomon, J.P. Suuronen, S.

Laboure, C. Guilloud, V. Valls, R. Barrett, E. Gagliardini, Y. Dabin, R. Baker, S. Bohic, C. Cohen, J. Morse, in *J. Synchrotron Radiat.*, International Union Of Crystallography**2016**, 344.

[68] M. Langer, A. Pacureanu, H. Suhonen, Q. Grimal, P. Cloetens, F. Peyrin, *PLoS One* **2012**, *7*, e35691.

[69] L. Weber, *Iterative Tomographic X-Ray Phase Reconstruction*, **2016**.

[70] D. Paganin, *Coherent X-Ray Optics*, **2006**.

[71] A. Mirone, E. Brun, E. Gouillart, P. Tafforeau, J. Kieffer, *Nucl. Instruments Methods Phys. Res. Sect. B Beam Interact. with Mater. Atoms* **2014**, *324*, 41.

[72] S. Schlüter, A. Sheppard, K. Brown, D. Wildenschild, *Water Resour. Res.* **2014**, *50*, 3615.

[73] A.P. Sheppard, R.M. Sok, H. Averdunk, in *Phys. A Stat. Mech. Its Appl.*, **2004**, 145.

[74] I. Arganda-Carreras, V. Kaynig, C. Rueden, K.W. Eliceiri, J. Schindelin, A. Cardona, H.S. Seung, *Bioinformatics* **2017**, *33*, 2424.

[75] W.E. Lorensen, H.E. Cline, *Comput. Graph.* **1987**, *21*, 163.

[76] X. Lu, T.M.M. Heenan, J.J. Bailey, T. Li, K. Li, D.J.L. Brett, P.R. Shearing, *J. Power Sources* **2017**, *365*, 210.

[77] S.J. Cooper, A. Bertei, P.R. Shearing, J.A. Kilner, N.P. Brandon, *SoftwareX* **2016**, *5*, 203.

[78] A. Gayon-Lombardo, L. Mosser, N.P. Brandon, S.J. Cooper, *Npj Comput. Mater.* **2020**.

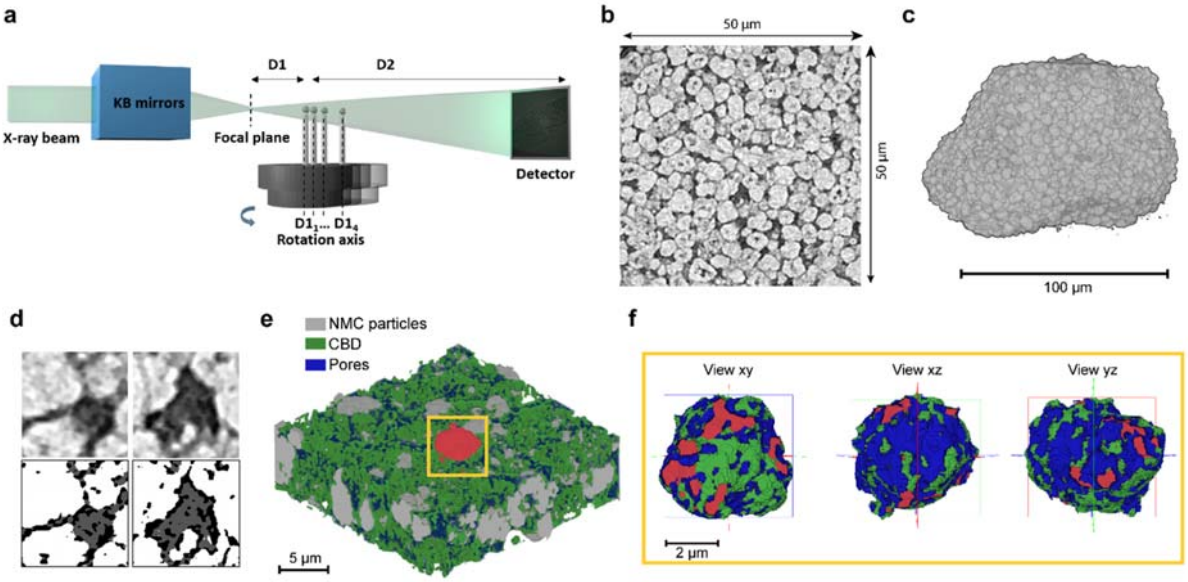

Figure 1. Illustration of the workflow used for this study. a. Schematic representation of the hard X-ray nano-holotomography experimental setup at ID16B [62] **b, c.** Raw data filtered with Non-local Mean and Unsharp Mask in 2D and 3D. **d, e.** Examples of the segmentation results in 2D and 3D using the machine learning segmentation plugin, Trainable Weka[74], in ImageJ. **f.** Visualization of the individual NMC particle colored in red in **e** along with the interfacial area with the other phases.

Table 1. Volume fraction of the active materials in the three electrodes. Expectation (Exp) values provided by the supplier are reported along with the values extracted from the 3D tomographic data (Data).

Sample	**MX-1**		**MX-1b**		**MX-2b**	
%v AM	Data	Exp.	Data	Exp.	Data	Exp.
	74.4	70.92	74.1	69.6	71.7	69.6

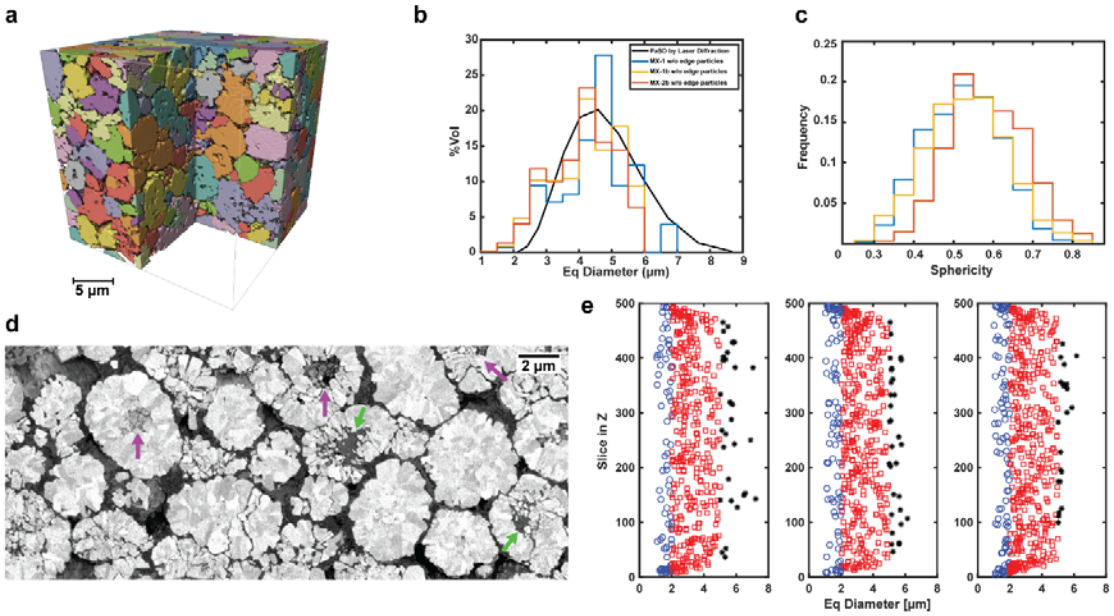

Figure 2. Morphology of the AM phase in three different samples. **a.** The AM phase of MX-1 sample is separated into individual particles that allow the statistical analysis of the microstructural properties by particles. **b.** Particle size distribution is given by tomographic data and by laser diffraction. **c.** The distribution of the sphericity of the NMC particles in the three samples. **d.** FIB/SEM image of the sample MX-2b shows cracked NMC particles. Purple arrows: internal pore without CBD, Green arrows: internal pore with CBD **e.** Spatial repartition of the NMC particles in the three samples in the direction normal to the current collector. Blue circles: Small particles, Red squares: Average particles and Black stars: Big particles.

Table 2. Microstructural properties of the CBD phase. Expected (Exp.) values are presented along with the values extracted from the 3D tomographic data (Data).

Sample	**MX-1**		**MX-1b**		**MX-2b**	
Percolation [%]	88.2		91.4		93.2	
%v CBD	Data	Exp.	Data	Exp.	Data	Exp.
	7.5	7.8	8.8	11.3	10.5	11.3
a_{CBD} [$\mu m^2 . \mu m_{CV}^{-3}$]	1.12		1.08		1.00	
σ_{e^-} [S.cm^{-1}]	0.0025		0.0250		0.0300	
E_a [eV]	0.030		0.007		0.006	

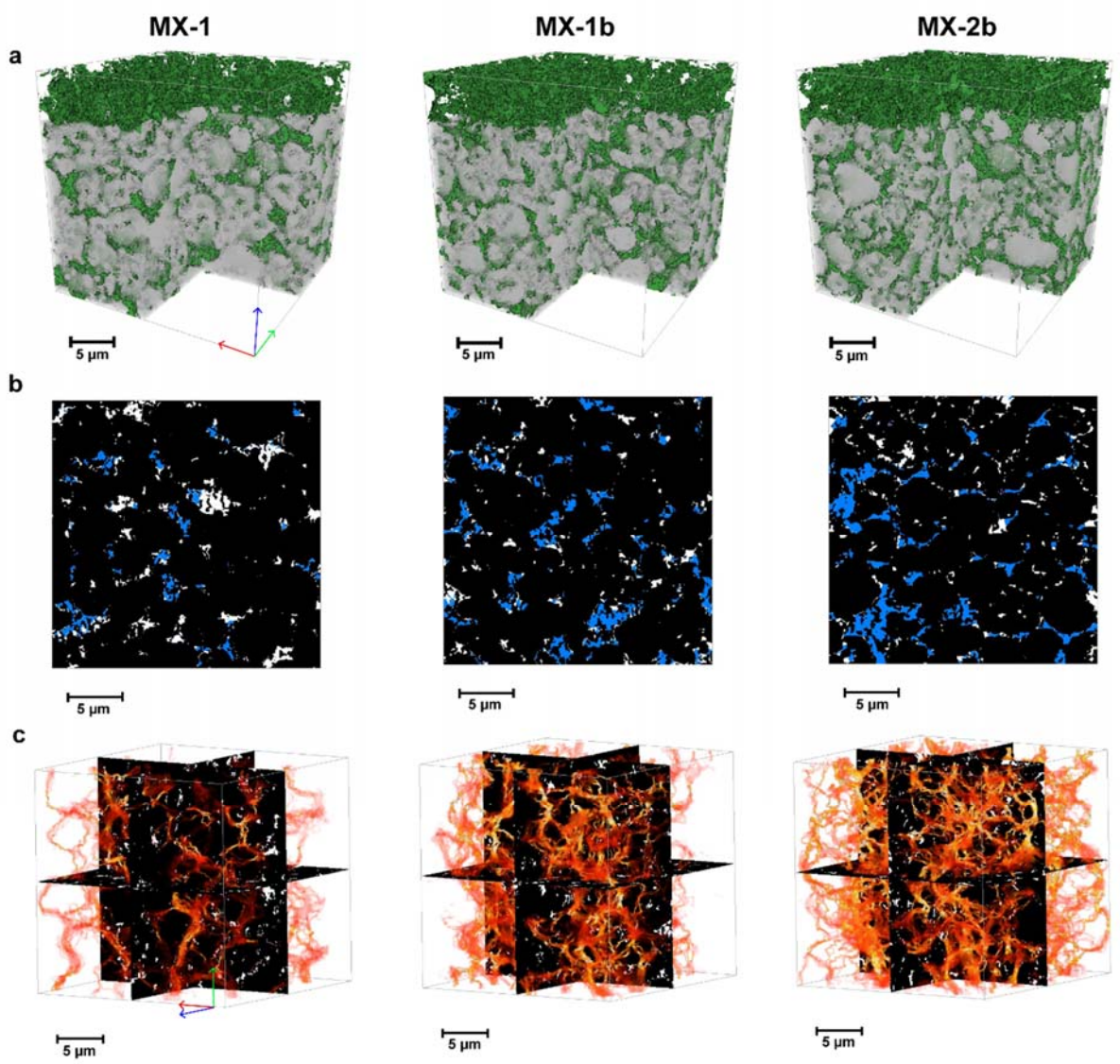

Figure 3. 3D microstructure of the CBD and simulations from diffusion-based method (with *TauFactor*) in the three different electrodes. a. The CBD network (green) within the control volume (25x25x25 µm^3). For the ease of visualization, the rest is represented as a transparent grey phase. **b.** For the ease of the observation of the porous morphology of the CBD, 2D slices are chosen to be shown, in which dead-end paths (white) and flux-through paths (blue) are both presented. One can observe the porous morphology of the CBD in various clusters (either in blue or white). **c.** The normalized flux density within the flux-through paths was colored for the three volumes. Dead-end pathways are represented in the three ortho slices as the white phase. Through-plane: Z-axis (green arrow), In-plane: X-axis (red arrow), Y-axis (blue arrow).

Table 3. Microstructural properties of the pore network. Expected (Exp.) values are presented along with the values extracted from the 3D tomographic data (Data).

Sample	**MX-1**		**MX-1b**		**MX-2b**	
Percolation [%]	95.5		94.6		94.6	
Porosity	Data	Exp.	Data	Exp.	Data	Exp.
	18.1	21.2	17.1	19.1	17.8	19.1
a_{pores} $[\mu m^2 . \mu m_{CV}^{-3}]$	1.05		1.07		1	
τ (N_M)	X-axis	Z-axis	X-axis	Z-axis	X-axis	Z-axis
	8.13 (45.17)	4.12 (22.88)	9.31 (54.44)	4.15 (24.15)	7.31 (41.07)	3.74 (21.05)
τ_e ($N_{M,e}$)	X-axis	Z-axis	X-axis	Z-axis	X-axis	Z-axis
	8.51 (47.28)	3.78 (20.87)	8.57 (50.12)	3.95 (22.99)	6.97 (39.16)	3.56 (20.00)

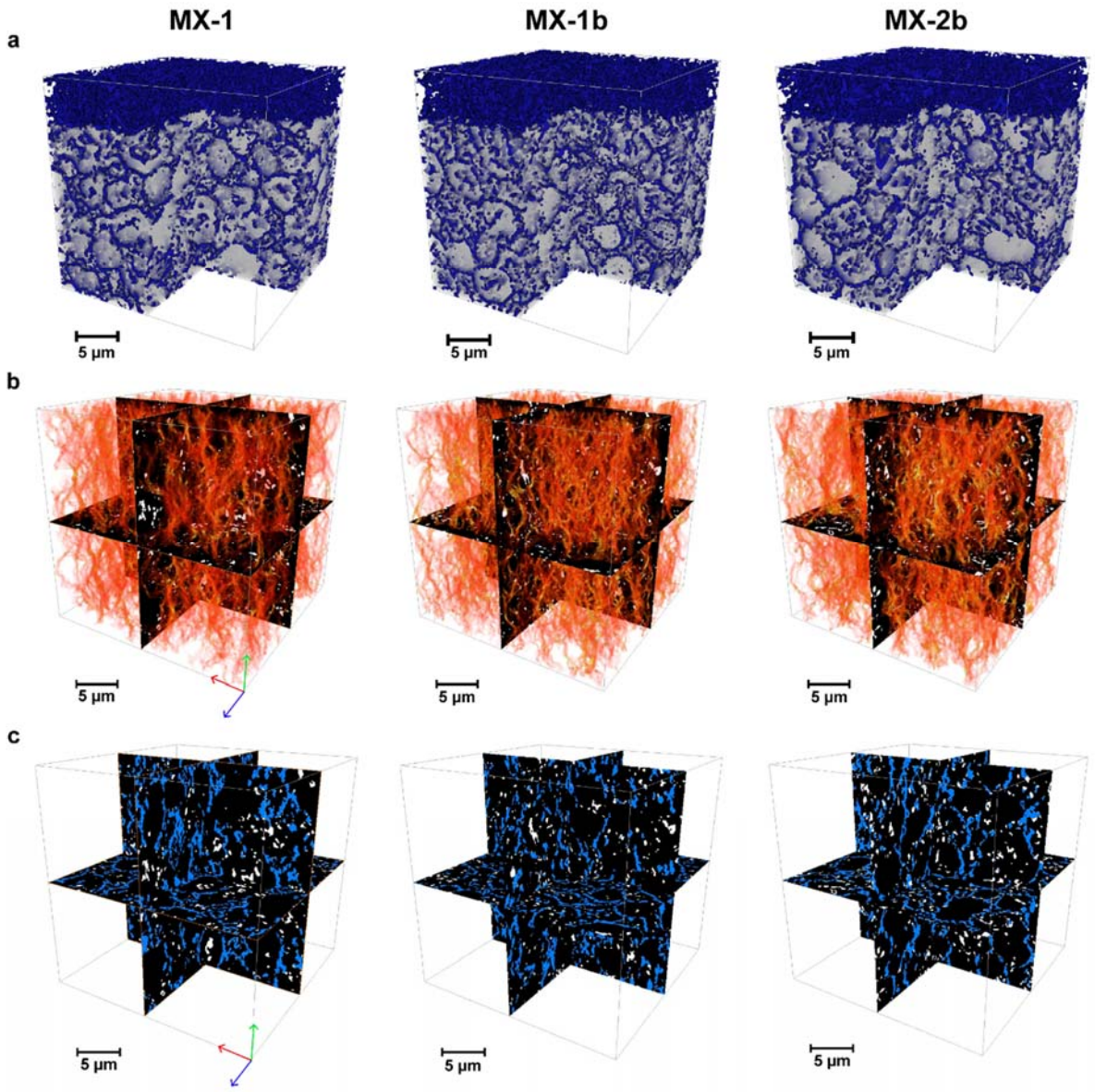

Figure 4. 3D microstructure of the pore network and simulations from diffusion-based method in the three different electrodes. a. Morphology of the pore network (blue) within the control volume, the AM & CBD phases are represented in transparent grey for the ease of visualization. **b.** The normalized flux density map of the pore network. The flux only passes by the through-pores in red, dead-end pores are represented in white on the ortho slices. **c.** The 2D ortho-slices of the pore network separated into through-pores (blue) and dead-end pores (white). Through-plane: Z-axis (green arrow), In-plane: X-axis (red arrow), Y-axis (blue arrow).

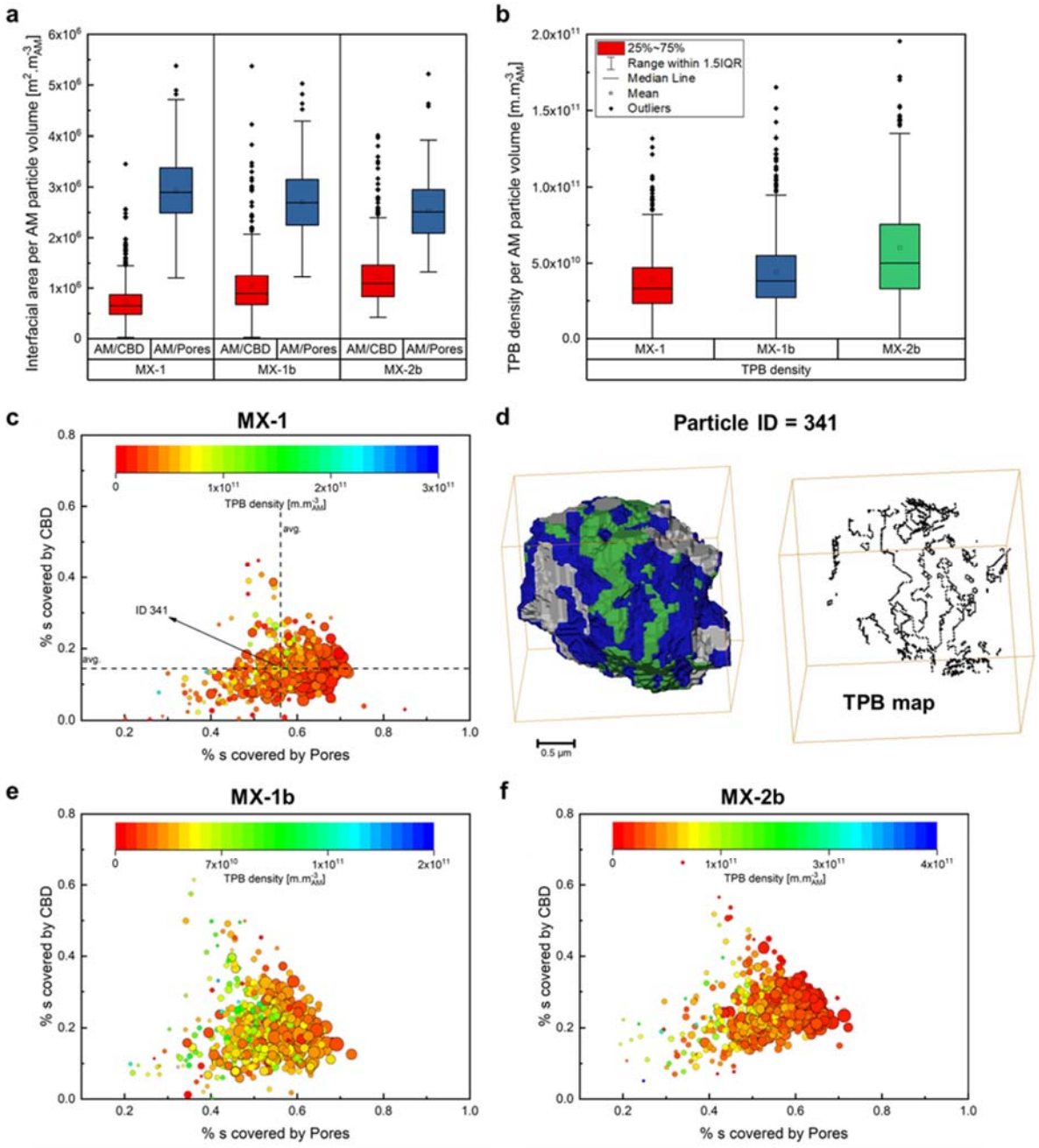

Figure 5. Inter-connectivity between phases in three samples. a. Interfacial area per AM particle volume between AM/CBD ($a_{P(AM/CBD)}$) and AM/pores ($a_{P(AM/pores)}$) are presented for each sample. **b.** TPB_p density per AM particle volume for each sample. **c, e, f.** Comparison of the distribution of different microstructural properties in three samples. The size of the dot corresponds to the particle size. The color corresponds to the TPB_p density of the particle, which is represented on the color bar. **d.** Visualization of the AM/CBD (green) and AM/pores (blue)

interfacial area along with the TPB map of the representative particle of sample MX-1 (ID=341). The dashed line to guide eyes cut each other at the representative particle.

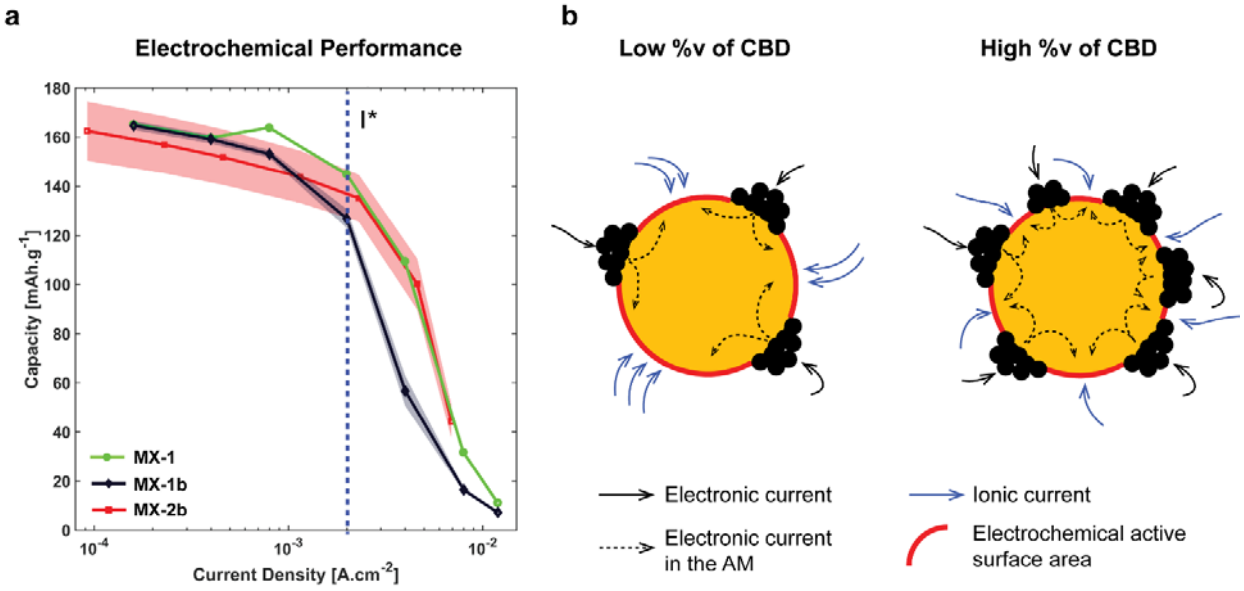

Figure 6. Correlation to the electrode performance. a. The lithiation performance of the three electrodes measured in a coin-cell setup at 25°C. The current density I* indicated the boundary between high and low current density regions. **b.** Our proposed scenario to explain the impact of the microstructure on the final performance. The electrochemical active surface area are highlighted in red. The excess of CBD increases the coverage by CBD over the AM particle surface as well as the TPB_p density but reduces significantly the interfacial area between AM and electrolyte filled in pores at which charge transfer takes place.

3D Quantification Of Microstructural Properties Of $Lini_{0.5}Mn_{0.3}Co_{0.2}O_2$ High-Energy Density Electrodes By X-Ray Holographic Nano-Tomography

Tuan-Tu Nguyen[1,2], Julie Villanova[5], Zeliang Su[1], Rémi Tucoulou[5], Benoît Fleutot[1,3], Bruno Delobel[2], Charles Delacourt[1,3*], Arnaud Demortière[1,3,4*]

Table of Content: Quantitative phase contrast X-ray nano-holotomography is used to capture the microstructures of different $LiNi_{0.5}Mn_{0.3}Co_{0.2}O_2$ high energy density electrodes. Microstructural properties are quantified along with their distribution through a statistical analysis at the particle scale. It allows understanding the performance of the electrodes and suggests new design to improve the power rate of these electrodes.

Table of Figures: